HYDRA: HYdrogel Dispensing with Robotic Automation for high throughput drug testing

Eloisa Torchia[1], Moises Di Sante[1], Bohdana Horda[1], Marko Mihajlovic[2], Julius Zimmermann[1], Melissa Pezzotti[1], Elisa Cimetta[3], Sylvain Gabriele[4], Ferdinando Auricchio[5], Johan Ulrik Lind[2], Alessandro Enrico[1,*], Francesco Silvio Pasqualini[1,*].

1. E. Torchia, M. Di Sante, B. Horda, J. Zimmermann, M. Pezzotti, A. Enrico, F. S. Pasqualini
   Synthetic Physiology Lab, Department of Civil Engineering and Architecture, University of Pavia, 27100, Pavia, Italy
2. M. Mihajlovic, J. U. Lind
   Department of Health Technology, Technical University of Denmark, 2800 Kgs. Lyngby, Denmark
3. E. Cimetta
   Department of Industrial Engineering, University of Padua, 35131 Padova, Italy
4. S. Gabriele
   Mechanobiology & Biomaterials Group, Research Institute for Biosciences, University of Mons, CIRMAP, 20 Place du Parc, Mons B-7000, Belgium
5. F. Auricchio
   Group of Computational Mechanics and Advanced Materials, Department of Civil Engineering and Architecture, University of Pavia, 27100, Pavia, Italy

E-mail: alessandro.enrico@unipv.it, francesco.pasqualini@unipv.it

Keywords: fish gelatin, HaCaT Keratinocytes, phase holographic imaging, nocodazole, paclitaxel

ABSTRACT

The poor predictivity of traditional cell culture platforms hampers drug research and development efficiency. While organoids and organs-on-chip mitigate this problem by introducing biomimetic in-vitro microenvironments in late pre-clinical stages, there is a lack of biomimetic platforms in earlier stages, particularly for high-throughput imaging screening (HTS). Something as simple as a thin hydrogel layer would provide physiological stiffness and native-like biochemical cues. However, casting hydrogels inside the small-diameter wells of HTS plates creates high-curvature menisci that negatively affect cell seeding and microscopy readouts. Here, we present a solution to this problem: HYdrogel Dispensing with Robotic Automation or HYDRA. This method allows automatic dispensing and aspiration of hydrogel precursors while preventing meniscus formation. Using this approach, we can produce gelatin hydrogels with tunable stiffnesses and thickness at room temperature and in commercial HTS plates. Then, we validate HYDRA in dose-response studies for anti-cancer drugs nocodazole and paclitaxel using genetically engineered epithelial cells (HaCaT) and imaging-based HTS readout methods such as phase holography and fluorescence microscopy. Taken together, this work shows that pharmaceutical companies can readily apply HYDRA with their current infrastructure to produce more biomimetic and predictive HTS platforms.

1 Introduction

Predicting how human cells will respond to new therapeutics accurately in preclinical stages is essential for enhancing drug research and development (R&D). However, this process has become notably lengthy, resource-intensive, and risky: typical efforts last ten years, cost over 1 billion US$, and fail nine out of ten times.[1] Genomics and artificial intelligence advancements have led to improvements,[2,3] but R&D still faces declining productivity and high failure rates in clinical trials.[4,5] It has been estimated that up to 50% of potential therapeutics that succeed in the initial preclinical assays fail in the following clinical trials, suggesting that existing preclinical models have a low capacity to predict human responses.[1,6] For example, drug development has relied on cell culture assay using plastic or glass substrates for decades. However, these stiff and inert substrates lack many physicochemical characteristics of soft and active biological tissues. These differences lead to loss of tissue-specific architecture, altered mechanical and metabolic signals, and distinct interactions between cells and their extracellular matrix (ECM). Together, these differences make traditional cell culture platforms poor preclinical models.[7]

Engineered cell culture systems provide conditions that better recapitulate the native in-vivo microenvironment, including substrate elasticity, proper anatomical architecture, and relevant mechanical stimuli.[8] For example, spheroids enable cell-cell and cell-ECM interactions in three dimensions and have recently been incorporated into automated high-throughput screening (HTS) infrastructure.[9,10] Moreover, organs-on-chip and organoids have been designed to capture the essential characteristics of various organs, model many diseases, and recapitulate in-vitro clinically relevant disease phenotypes and pharmacological responses.[11] Organs-on-chip offer microenvironmental control and the ability to assess tissue structure and function, but engineering challenges persist in producing them at a scale compatible with HTS.[8] Similarly, organoids offer physiologically relevant and anatomically accurate cell types but typically lack perfusing blood vessels, which must be added to more complex microfluidic channel engineering.[12–14] Finally, the 3D nature of organoids and spheroids makes quantitative structure and function studies challenging in imaging-based HTS.[8]

We reasoned that a planar hydrogel bed for cell seeding would bridge the gap between current 2D-optimized HTS pipelines and more physiological yet too complex 3D models. Hydrogels have been used to prepare organoids and organs-on-chip and allow the tuning of chemical and mechanical properties of the resulting tissues.[15] Moreover, hydrogels are optically transparent and allow standard imaging setups and analysis pipelines for live cell imaging or via immunofluorescence.[16,17] Yet, contrary to conventional cell culture materials like plastic and glass, 2D hydrogel-based systems offer precise control over crucial environmental factors such as substrate stiffness, making these platforms well-suited for investigating cell viability and behavior.[18] And yet, realizing planar hydrogels inside HTS platforms is challenging. The profile of the hydrogel precursor solution is dominated by the capillary forces at the sidewalls of the small-diameter wells, leading to the formation of a high curvature meniscus at the air-liquid interface during casting that interferes with cell culture and imaging techniques.[19]

Several researchers have focused on developing 2D hydrogel-based engineered platforms integrating high throughput formats and automated liquid handling. For instance, Brooks et al. described 2D PEG-based hydrogel fabrication at the bottom of a 96-well plate, obtaining hydrogel substrates with tunable stiffness.[20] Hydrogels were easily formed within the microplate using photo-crosslinking in the first approach. However, the resulting hydrogel thickness ranged from 500 to 1000 µm, which can limit the application of high-resolution imaging techniques. Instead, Machillot et al. presented a film-coated microplate using the layer-by-layer technique.[21] However, this method yielded much thinner hydrogel layers, typically just a few microns thick, which are insufficient to prevent cells from feeling the under underlying high substrate stiffness, influencing their behavior.[22]

Here, we present a scalable and automated method for fabricating planar hydrogels with proper thickness suitable for cell-based high throughput and imaging applications. To avoid meniscus formation, we developed and optimized a routine to dispense and re-aspirate hydrogel precursors to prevent the solution from contacting the walls. We called the method HYDRA: HYdrogel Dispensing with Robotic Automation. We created 10-50 µm-thick gel layers on the well bottom by dispensing and re-aspirating the hydrogel precursor solution using a liquid handling robot (**Figures 1A and B**). We used microbial transglutaminase (TG) and cold fish gelatin (FG) as they remain liquid at room temperature (**Figure 1C**).[23] Then, we showed that HYDRA 96 and 384 HTS well plates can be used for drug testing with digital holography and

fluorescence microscopy using human epithelial cells (HaCaT) genetically engineered to express various fluorescent sensors (**Figures 1D, E, and F**).[24]

Our results show that leveraging existing automated liquid handling robots and microscopes commonly found in HTS facilities can create a new foundation for engineering cell culture platforms that pharmaceutical companies may adopt more easily.[8]

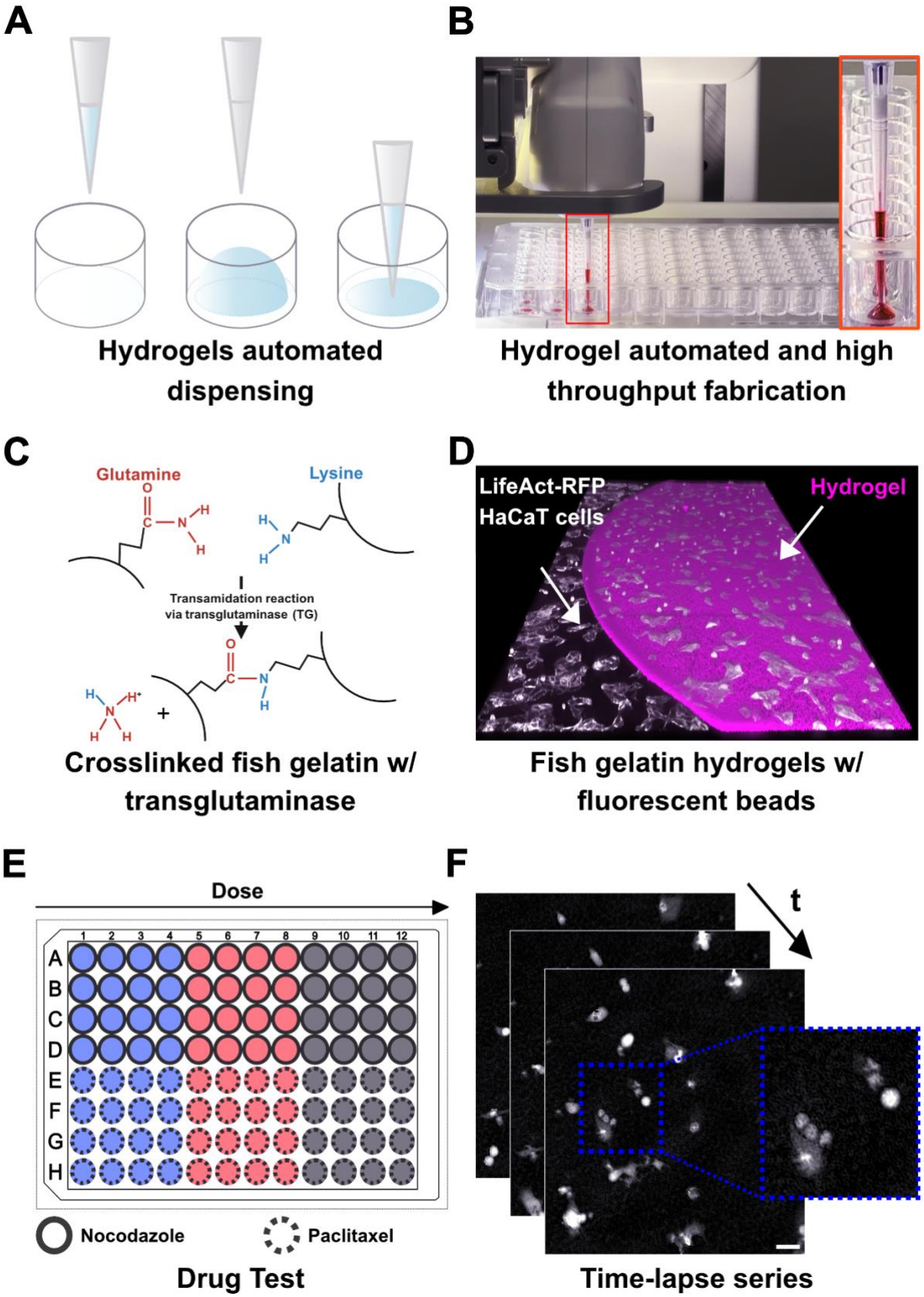

Figure 1. HYdrogel Dispensing method with Robotic Automation (HYDRA) for HTS-compatible hydrogels. A) Schematic illustration of the Hydrogel Dispensing with Robotic Automation (HYDRA) method. **B)** Photograph of the robot performing the HYDRA of fish gelatin (FG) hydrogels in a 96-well plate. A red food colorant was added for visualization

purposes. **C)** Schematic of FG crosslinked with microbial transglutaminase (TG). Glutamine residues in proteins can form covalent bonds with lysine residues through a transamidation reaction, which produces ammonia as a byproduct. In this process, the γ-carboxamide groups of glutamines serve as acyl donors, while the ε-amino groups of lysine function as acyl acceptors. Created using Biorender.com. **D)** Isometric confocal z-stack (3D rendering) of a HYDRA-fabricated FG hydrogel embedding fluorescent beads and HaCaT cells seeded on top and on the side of the hydrogel. **E)** Schematic representation of drug tests performed with nocodazole and paclitaxel. Drug dose (three concentrations of each drug color-coded as blue – low concentration, red – medium concentration, and black – high concentration) increases along columns. **F)** Time-lapse holographic images of HaCaT cells on hydrogel substrates acquired during 48 hours of treatment with nocodazole or paclitaxel. Scale bar: 50 μm.

2 Results and Discussion

Rheological studies of fish gelatin hydrogels.

We crosslinked FG chemically using TG to fabricate hydrogel-based cell culture platforms with HYDRA (Figure 2A).[25,26] Critically, we selected FG since aqueous solutions of FG remain liquid at room temperature (RT) and must be cooled to 4 °C to form a physical gel. The viscosity of FG should thus stay low and stable at RT to make dispensing possible.[27] To test this hypothesis, we used oscillatory rheometry to evaluate the properties of FG mixtures, optimize the casting of FG hydrogels in 96 well plates, and quantify the mechanical properties of the casted gels. Specifically, we analyzed FG viscosity at RT to ensure compatibility with the liquid handling robot. The viscosity at zero shear rate measures the material's viscosity at rest, and we observed this measure doubling in our precursor solution when we doubled (from 0.67 ± 0.18 to 2.11 ± 0.06 Pa·s) the FG concentration (Figure 2B), in good agreement with the literature.[26,28] Still, unlike gelatin solutions obtained from mammalian sources, it remained below the threshold for pipettability with air displacement pipettes.[29–31]

The gelation point of the FG hydrogels is expected to decrease with higher polymer concentration.[26] To test FG pipettability across a more extensive range of conditions, we examined FG physical gelation using the tube inversion method. Specifically, we prepared three FG concentrations (5% w/v, 10% w/v, and 20% w/v in PBS -/-) to generate gels with physiological stiffness when mixed with TG.[28] We dispensed FG solutions into microcentrifuge tubes, placed them at RT and 4 °C for 72 hours, and took pictures after 24 hours upon inversion (Figure S1). All the mixtures flowed with gravity except for the 20% FG mixture at 4 °C, for which viscosity was high enough to counter the gravitation pull, Furthermore, we analyzed chemical gelation by crosslinking gelatin solutions with 2% w/v TG at RT and 4 °C for 72 hours. Independent of temperature and concentration, all FG solutions formed gels within 72 hours (Figure S1).[26] These results show that, in principle, a liquid-handling robot can dispense FG solutions at room temperature.

To establish an appropriate automated protocol in which gelation occurs after liquid handling is completed across the entire plate, we sought to understand the gelation initiation time (onset

time). For this reason, we evaluated the crosslinking kinetics of 10% w/v FG hydrogel with TG concentrations (0.5% w/v and 2% w/v). The range of TG values was chosen based on reported values optimized for bioprinting.[32] Both TG concentrations resulted in a gradual crosslinking process (**Figures 2C and D**). Specifically, the storage modulus (G') and loss modulus (G'') curves associated with 0.5% w/v TG suggests that crosslinking proceeds more slowly at this concentration (**Figure 2C**). In comparison, the curves for 2% w/v TG reached a plateau approximately 3 hours after mixing (**Figure 2D**). For 10% w/v FG hydrogels crosslinked with 2% w/v TG, the crossover point was reached after about 40 minutes, suggesting the rapid blending of the two components in an HTS plate format should not trigger partial gel formation.

Finally, we evaluated whether the selected concentrations yielded substrates with stiffness within a physiological range by measuring the shear modulus of our hydrogels. (**Figures 2E and F**). Samples crosslinked with 2% w/v TG exhibited G' ranging from 500 Pa to 3 kPa (**Figure 2E and Figure S2**), again in good agreement with the literature.[26] Finally, to understand the TG effect on the resulting hydrogel stiffness, we used a gelatin concentration of 10% w/v and varied TG concentrations from 0.5% to 2% w/v (**Figure 2F, Figure S2C-D, and S3**). We found the value G' increasing (from 500 Pa to about 2 kPa) with increasing TG concentration (**Figure 2F and Figure S3**). This trend and the G' values align with previous works reporting on fish gelatin hydrogels chemically crosslinked at 37 °C.[33] Together, these results demonstrated the viscosity of fish gelatin at room temperature can be managed using a liquid handling system, even with high protein concentrations (20% w/v). We also found that the dispensed hydrogels display physiologically relevant stiffness when cross-linked by TG.

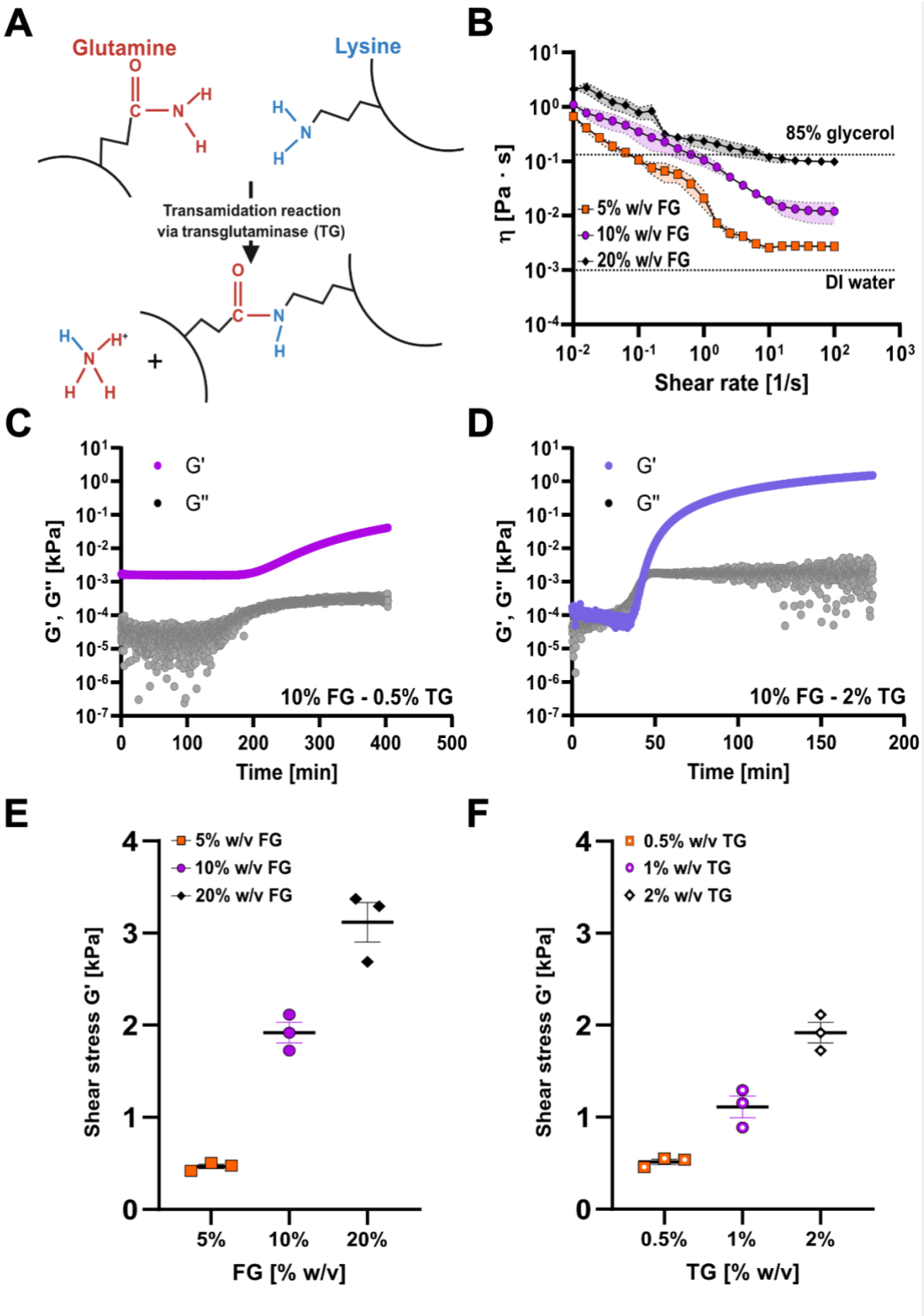

Figure 2. Rheology of fish gelatin hydrogels. A) Schematic of FG hydrogels chemically crosslinked with TG. Glutamine residues in proteins can form covalent bonds with lysine residues through a transamidation reaction, which produces ammonia as a byproduct. In this process, the γ-carboxamide groups of glutamines serve as acyl donors, while the ε-amino groups of

lysine function as acyl acceptors. Created with Biorender.com. **B)** Viscosity vs. shear rate for three different concentrations of FG alone (5% - orange squares, 10% - purple dots, and 20% w/v - black diamonds). Dashed lines stand for viscosity values for 85% glycerol and deionized water at room temperature. **C)** G' and G'' vs. time for FG at 10% w/v concentration crosslinked with 0.5% w/v TG. **D)** G' and G'' vs. time for FG at 10% w/v concentration, cross-linked with 2% w/v of TG. Data are displayed as mean ± s.e.m (n=3 samples). **E)** Shear modulus G' vs. FG concentration (5% - orange squares, 10% - purple dots, and 20% w/v - black diamonds). FG solutions were crosslinked with 2% w/v TG. Data are displayed as mean ± s.e.m (n=3 samples). **F)** Shear modulus G' vs. TG concentration (0.5% - orange squares, 1% - purple dots, and 2% w/v - black diamonds). 10% w/v fixed FG was used. Data are displayed as mean ± s.e.m (n=3 samples).

Modeling, fabrication, and characterization of hydrogel thin film in 96-well plates.

To optimize the fabrication step – that is, to minimize meniscus formation while maximizing well coverage - we modeled the meniscus formation process using a finite-element modeling (FEM) approach in COMSOL. First, we simulated a classical meniscus-formation scenario in which the dispensed volume caused wetting of the sidewalls (**Figure 3A**; **Video S1**). Then, we computed the ratio between the radius of the hydrogels with the air-liquid interface being parallel (± 3 degrees) to the substrate and the radius of the well. This configuration led to the gel covering the entire area of the well (100% radial coverage), but the high curvature meniscus severely limited the available planar area (10% flatness). Then, we repeated the simulation, reducing the volume to avoid touching the walls and thus forming the meniscus. In this case, we applied a receding angle correction to simulate the pinning of the contact line during re-aspiration (**See Video S2**).[34] To select a volume that maximizes gel flatness, we compared the profile obtained with four different nominal volumes (6 µL, 12 µL, 18 µL, and 24 µL). In the absence of a wall meniscus, gel coverage and flatness increased with increasing volumes, with 18 µl producing the highest flatness. Using 24 µl resulted in wall wetting, significantly limiting the planar portion of the resulting gel. To account for the fabrication non-idealities, we also introduced small fluctuations in simulation parameters: ±20% on dispensed volume; -100 µm and -200 µm on well radius because of the fabrication tolerance of the well plate and the accuracy of the robot. Considering these fluctuations, we verified that dispensing 18 µL may result in wall wetting (See **Figure S4**). Therefore, we selected 12 µL for the experiments in this manuscript: which reduced coverage by ~20% and increased flatness by 4.5 times with respect to the meniscus-inducing conditions (**Figure 3B and Figures S4**).

Based on these results, we fabricated FG hydrogels automatically in a 96-well plate format using an Integra liquid handling robot. We used a mixture of FG and TG with a red food colorant to simplify the visualization. We aspirated 12 µL hydrogel precursor solution and dispensed it in each well along columns. Then, the same amount of solution was re-aspirated from each well in sequence, leaving only a boundary layer of hydrogel precursor to set. The procedure took about 10 minutes, roughly a quarter of the 40-minute threshold we established with rheometry (**Figure 3C; Video S3 and S4**).

Next, we characterized the thickness and flatness of hydrogel thin films to understand if these dimensions are compatible with standard imaging instruments. To do so, we embedded

fluorescent beads inside the gel to visualize its thickness with confocal microscopy. We seeded epithelial cells featuring a red, fluorescent actin marker (Life Act™) on the substrate to visualize both the bottom of the well and the top of the gel-free surface (**Figure 3D**). Using a 20X air objective (NA 0.75), we captured two images – one at the top of the gel and another at the bottom of the well - by focusing on cell actin and the fluorescent beads. The samples exhibited an expected dose-dependent increase in thickness, from ~10 µm to ~30 µm, and inter-group reproducibility (**Figure 3E and Figure S5**). This result agrees with the literature, which sets the cut-off point for how deeply cells sense substrates at 10-20 µm.[22] Together, these results support that liquid handling automation can reproducibly form thin hydrogel layers for cell culture in commercial HTS plates.

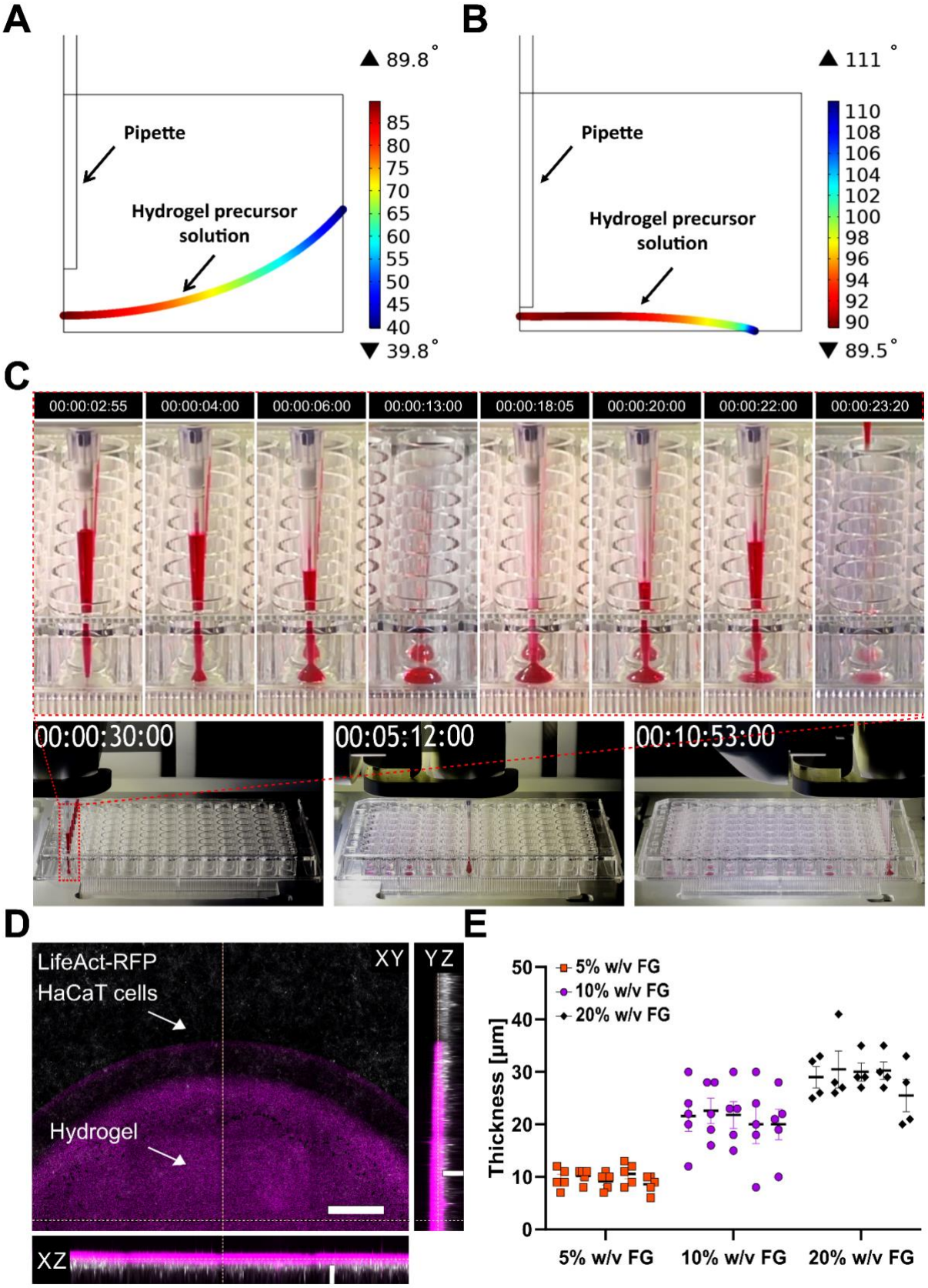

Figure 3. Hydrogel Dispensing with Robotic Automation (HYDRA) fabrication method. **A)** 2D representation of hydrogel profile angles resulting from COMSOL simulation after **A)** conventional casting, displaying meniscus formation, and **B)** HYDRA casting. **C)** Sequential frames illustrating the fabrication of FG hydrogel thin films using a commercial high

throughput plate and liquid handling robot. Sequential frames of a zoom on a single well are displayed on top. **D)** 2D reconstruction of hydrogel profile embedding fluorescent beads (in magenta) and with HaCaT cells (in gray – RFP-Life Act™) seeded on top. The z-stack of the hydrogel volume was acquired using confocal imaging. A max intensity projection was applied to the orthogonal views. XY plane scale bar: 200 μm. Orthogonal views (XZ, YZ) scale bars: 20 μm. **E)** Assessment of thickness and flatness of FG hydrogels at three different concentrations (5% - orange squares, 10% - purple dots, and 20% w/v – black diamonds) in a hydrated state. The data correspond to a single experiment (3 concentrations, n=5 samples for each concentration). For each sample, 5 FOVs were taken to measure the z-position and calculate thickness. Data are presented as mean ± s.e.m.

Drug testing using digital holographic for long-term imaging.

To show that HYDRA HTS platforms can be used for testing drugs, we seeded human epithelial cells (HaCaT) sparsely on the gels to assess proliferation. Then, we exposed them to nocodazole and paclitaxel, compounds with known cell cycle inhibitory effects.[24,35,36] The primary aim was to highlight the feasibility of integrating hydrogel-based cell culture platforms into imaging-based drug screening systems. To challenge HYDRA, we first tested its performance in a long, live-cell imaging experiment using digital holography. Digital holography is a technique with minimal phototoxicity but relies on accurately detecting small changes in the refractive indexes of cells and substrates.[37] Having added a thin hydrogel layer to provide a more biomimetic microenvironment for the cell with HYDRA, we asked whether digital holography could still pick up a significant enough refractive index change. Further, we used cell culture plastic 96-well plates for this stress test, which have poorer optical properties than HTS plates designed for imaging experiments. Moreover, the digital holography experiments were conducted inside the cell culture incubator for 48 hours.

We explored the range of drug concentrations known in the literature to affect the HaCaT cell cycle.[35,36] Specifically, we opted for three concentrations of nocodazole (12.5, 25, and 50 ng/mL, shown in **Figures 4A**, **4B**, and **4C**) and three concentrations of paclitaxel (0.5, 2.5, and 12.5 ng/mL paclitaxel, shown in **Figure S6A**, **B**, and **C**). We include vehicle controls (0.1% DMSO in full culture media), where we expected to see no effect on the cell cycle, as well as positive controls, in which cells were exposed to a deadly concentration of an antibiotic to which HaCaT cells were not resistant (geneticin). The experiment was conducted twice, and cells were seeded either on the FG gels or directly on the plastic plate. We successfully performed holographic imaging on HYDRA-prepared hydrogels, identifying the presence and shapes of the cells (**Figure 4A, 4B, 4C, Figures S6, S7, and S8**; see also **Video S5 and S6**) and extending the applicability of phase microscopy from low-throughput hydrogels[38] to HTS.

Moreover, since we imaged all wells every hour for 48 hours, we analyzed time-lapse images to measure the total area covered by cells, referred to as '% confluency.' This parameter is important since proliferating cells will increase their confluency over time, and compounds expected to arrest the cell cycle would ideally delay or arrest this increase (**Figure 4D, S6D, and S8D-E**). When we compared the confluency after 48 hours of cells on plastic surfaces and those on hydrogels (**Figure 4E**) we saw that cells subjected to nocodazole exhibited

different physiological behaviors on gels compared to plastic surfaces. We observed a comparable trend in paclitaxel-treated cells on both plastic and hydrogels (**Figure S6E**). Specifically, cell confluency decreased on both plastic and gel surfaces as the drug dosage increased, indicating a higher cell cycle blockage (**Figure 4E and Figure S6E**). In both scenarios, the final cell confluences on hydrogels were twice those observed on plastic, highlighting the importance of more biomimetic substrates. We also quantified IC50 drugs in the case of plastic or hydrogel substrate: about 17 ng mL^{-1} on plastic and 18 ng mL^{-1} on hydrogel in the case of nocodazole, 1.6 ng mL^{-1} on plastic and 1.8 on hydrogel in the case of paclitaxel (**Figure 4F and Figure S6F**). While yielding similar IC50 values, the proliferation kinetics of HaCaT cells on hydrogel or plastic differed, which is also in good agreement with the literature.[39] Together, these results support the notion that HYDRA HTS platforms can provide more biomimetic support for cell proliferation and still be integrated with advanced imaging capabilities and standard analysis pipelines for drug testing applications.[39]

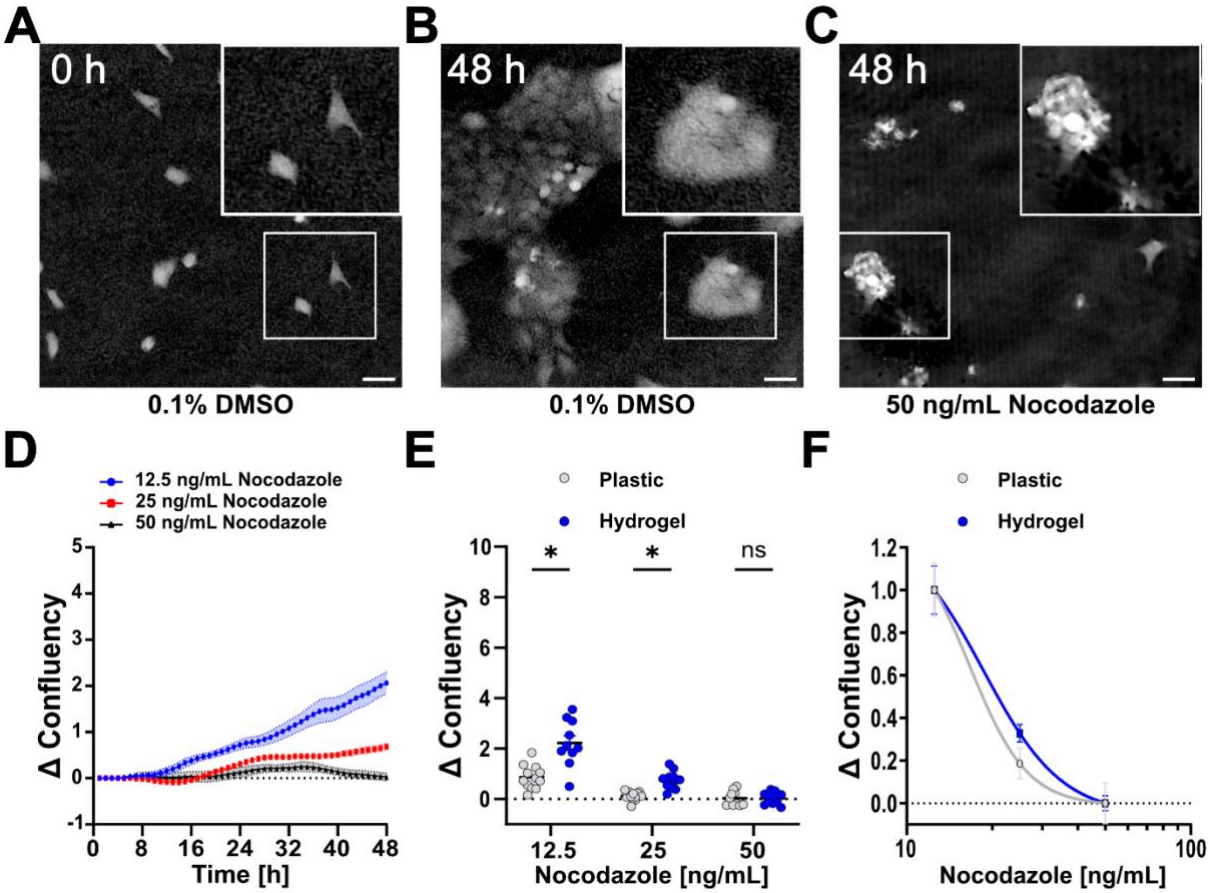

Figure 4. Drug test using phase holographic imaging. A) Holographic image of HaCaT cultured in 0.1% DMSO – vehicle control – after seeding and **B)** 48 hours after seeding. **C)** Holographic image of HaCaT treated with 50 ng mL^{-1} of nocodazole drug 48 hours after seeding. Scale bars: 50 µm. **D)** HaCaT cell confluency vs. time. Cells were cultured in nocodazole-based cell culture media (12.5 ng/mL – blue dots, 25 ng/mL – red squares, 50 ng/mL black triangles) for 48 hours on hydrogel substrates. Data were normalized concerning the initial confluency value. Solid lines represent mean values, and shaded areas represent s.e.m (n=12). **E)** Final cell confluency vs. nocodazole concentration (12.5 ng/mL, 25 ng/mL, 50 ng/mL) on plastic and hydrogel substrates. Data were normalized concerning the initial confluency value. (*) stands for significative difference. **F)** Nocodazole dose-response curves on plastic (IC50, 16.6 ng mL^{-1}) and hydrogel (IC50, 18.1 ng mL^{-1}) substrates (n=12). Data were normalized concerning the initial confluency value (n=12). Image brightness and contrast were adjusted for printed visibility.

Drug testing assay using standard fluorescence static imaging.

Next, we sought to validate the applicability of HYDRA plates to fluorescence microscopy and confirm that the digital holography results we obtained were consistent with the known mechanisms of action of the drugs used. Nocodazole and paclitaxel influence cell cycle progression by modulating microtubule dynamics, arresting the cell cycle before division (or M-phase), and eventually leading to cell death by apoptosis.[40–42] To examine the effects of these drugs on the cell cycle, we used HaCaT cells genetically engineered to express fluorescent sensors for the cytoskeletal proteins actin and tubulin, as well as our novel cell cycle sensor FUCCIplex. (**Figure 5A**). [24]

In this set of experiments, we used fluorescence microscopy with a temperature and CO_2-controlled incubator to repeat the same drug test performed using holographic imaging. Specifically, we used HYDRA to cast gelatin hydrogels on plastic 96-well plates. Then we counted M-phase arrested cells on hydrogels or plastic in the presence of the two compounds 24 and 48 hours after administration (**Figure 5B - iii and Figure S9 - iii**). First, we confirmed that fluorescence imaging is compatible with HYDRA-casted hydrogels like holographic imaging in the preceding section. Second, we looked for evidence of the drug effect. Cells treated with the highest nocodazole drug concentration displayed nuclear fragmentation (**Figure 5B - iv**), typically associated with cellular damage before apoptosis.[43] For this reason, cells with a nuclear area smaller than the mean nuclear area of control cells were excluded from the analysis. Then, by counting the fraction of cells undergoing cell division, we showed the expected dose-dependent accumulation of arrested cells in the nocodazole-treated group (**Figure 5B - v**).[35,36] Further, we observed nuclear fragmentation (**Figure S9 - iv**) and a comparable trend regarding the number of cells undergoing mitosis in paclitaxel-treated samples (**Figure S9 - v**).[43]

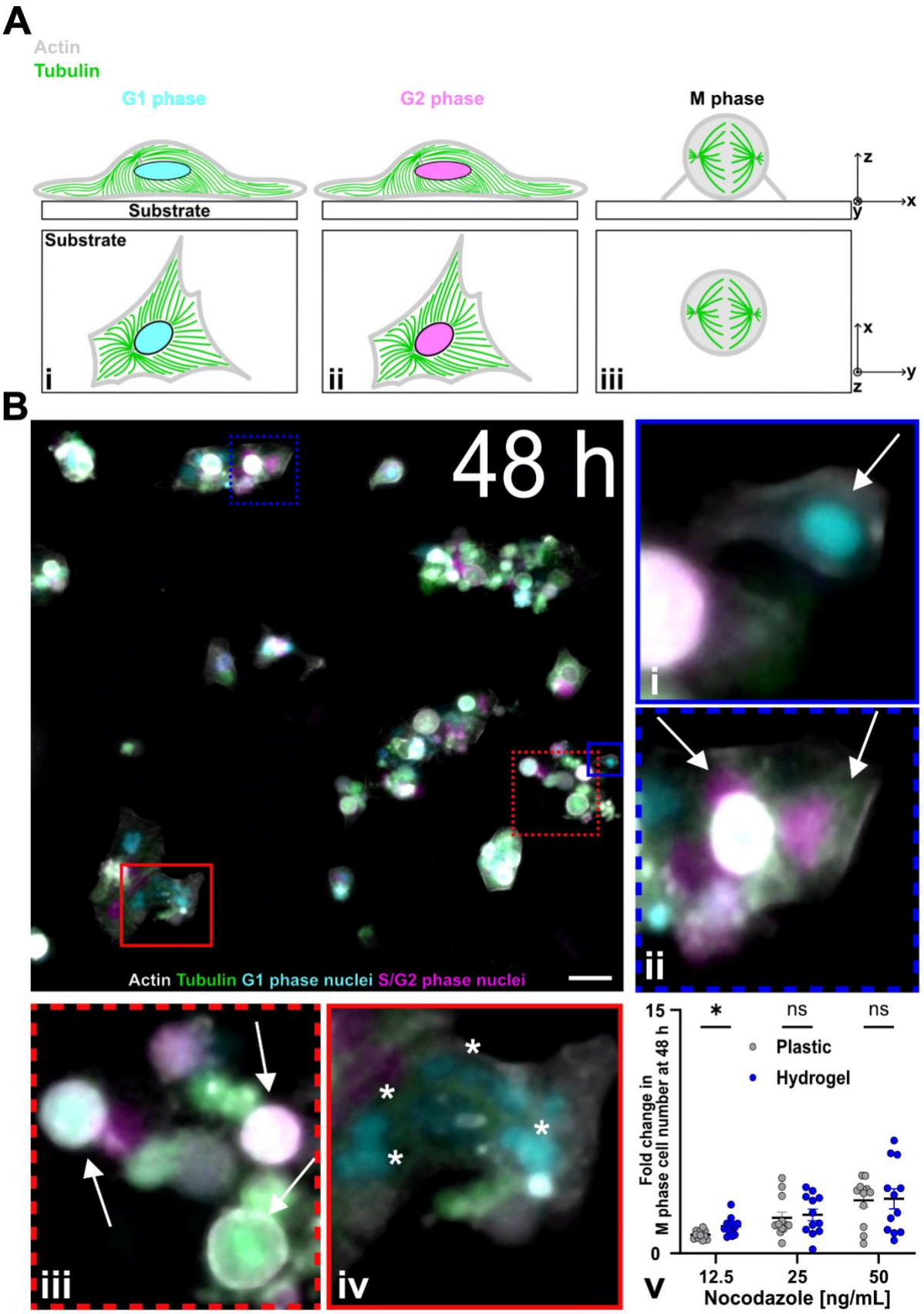

Figure 5. Drug test using static fluorescence imaging on 10% w/v fish gelatin hydrogels. A) Schematic illustration of cell-substrate interaction during the cell cycle. A cell in **i)** G1 or in **ii)** S/G2 phase exhibits a degree of spreading based on the substrate. During iii) the mitosis (M) phase, the phase before cell division, the cell undergoes rapid internal architectural

changes, assuming the characteristic spherical shape associated with mitotic cells. **B)** Static widefield images of HaCaT (RFP – Life Act in gray, GFP – tagged tubulin in green) 48 hours after seeding. Cells were treated with 50 ng/mL nocodazole. Arrows stand for **(i)** cells in the G1 phase (in cyan), **(ii)** cells in the S/G2 phase (in magenta), and **(iii)** cells in the mitotic (M) phase. Asterisks stand for **(iv)** nuclear fragmentation. **(v)** Fold change in M phase cell number after 48 hours vs. nocodazole concentration on plastic and hydrogel substrates. Cell number in the M phase was counted as a fraction of the total cell number in a FOV and then normalized to the vehicle negative control (n=12). Data are displayed as mean ± s.e.m. (*) stands for statistical difference. Images were taken on hydrogel thin layers cast on plastic plates. Scale bar: 50 μm.

HYDRA 384-well plate.

Finally, we asked whether the HYDRA method could be scaled to other high-throughput formats, such as a 384-well plate, and higher resolution imaging modalities using plates with a high-refractive index cyclic olefin copolymers (COC) backing. With a working volume of 1 µL, HYDRA prevented meniscus formation by avoiding contact with the walls of each well. With such a small volume, we used 10% w/v FG and 0.5% w/v TG to reduce precursor viscosity and optimized dispensing so that the entire plate could be completed in approximately 10 minutes. Given the large number of prepared wells, we developed an automated quality control procedure for HYDRA plates that acquires and analyzes the 384 wells in less than two hours (**Figure 6A** and **Video S7** and **S8**). First, we took fluorescence images of the embedded beads with a 4X objective (NA 0.13) in confocal mode. Second, we calculated max intensity projections to determine whether the gel touched the walls (red box) or if the intensities were inhomogeneous (yellow box). Our quality control revealed a ~90% yield (green box) with only 6% unusable meniscus profiles (**Figure 6A**, red box) and partially usable concave gels (yellow box) (**Figure 6A**). We further characterized a sample of inhomogeneous gels with higher resolution Z-stacks to confirm their non-planar profile (**Figure S10A-B**). For comparison, our quality control revealed a yield of less than 10% for 1536-well plates since liquid handling robots for this format have higher positioning precision and lower liquid handling volume capabilities than ours (**Figure S10C**).

Finally, we demonstrated how HYDRA 384 well plates can be used in advanced fluorescence microscopy applications as required by modern imaging-based HTS approaches (**Figure 6B**).[44] First, we performed live-cell imaging experiments by following HaCaT cell proliferation for 18 hours on multiple field-of-views using a 40X silicon oil objective (NA 1.25) and a perfect focus system (**Figure 6C** and **Video S9**). The image quality was high enough to enable semi-automated segmentation and tracking with modern AI-based image analysis software such as Stardist and TrackMate (**Figure 6C**).[45,46] Finally, to show that the gels do not prevent the assessment of fine ultrastructural details, we performed high-resolution confocal acquisitions with a 100X silicon oil objective (NA 1.35) (**Figure 6D**). In the same field of view, we could observe how the microtubule organization changes from a mostly planar network in adhered and spread-out cells(**Figure 6D - i**) to a mitotic spindle during cell division (**Figure 6D - ii**).

Together, our results show that HYDRA can be used on various well-plate formats, from low throughput to HTS, and substrates, from glass to plastic, where it remains viable for two months (**Figure S11**). In all these scenarios, HYDRA enables HTS with multiple imaging modalities.

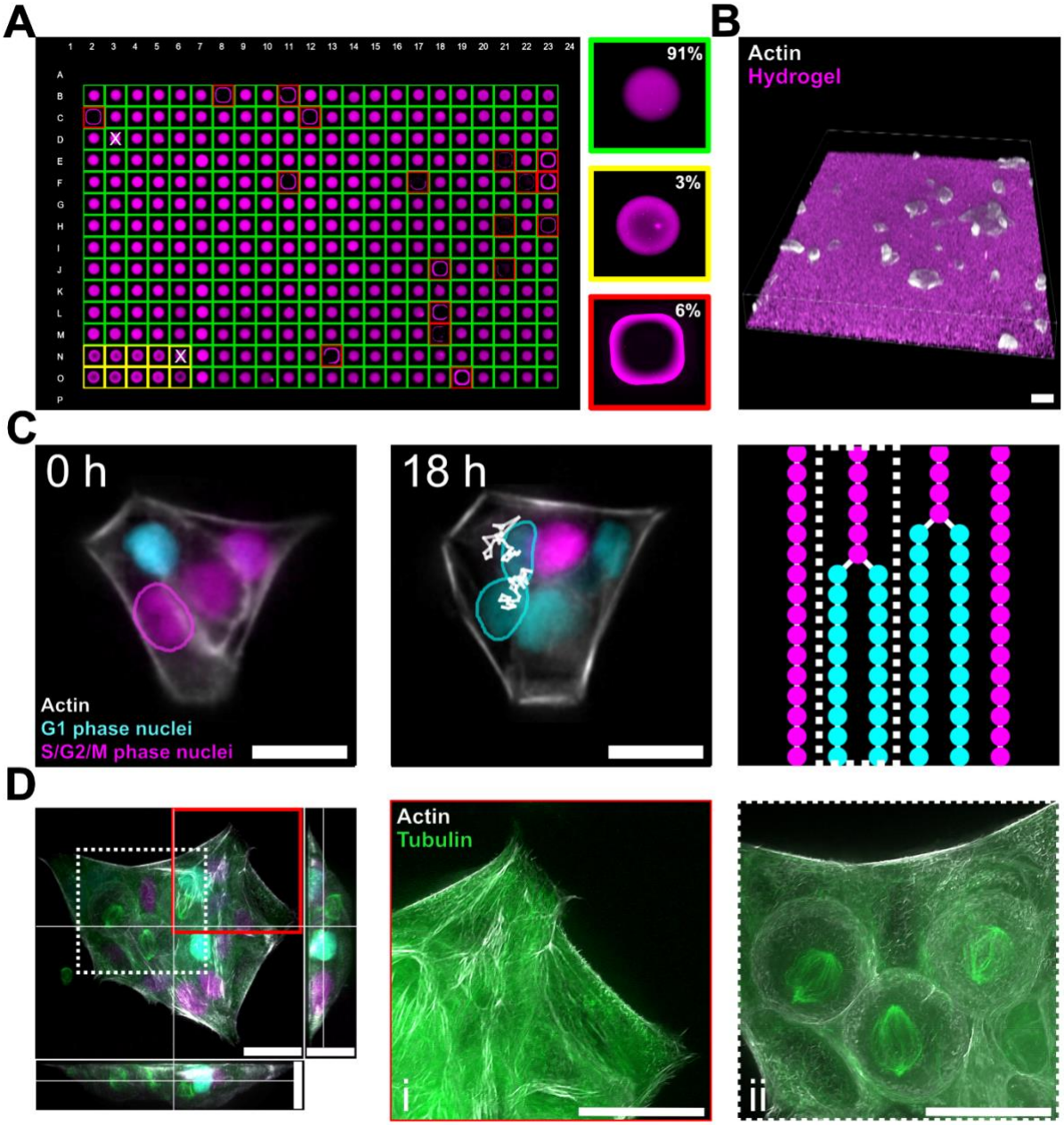

Figure 6. HYDRA-like hydrogels on a 384-well plate. (A) Hydrogels cast in a 384-well plate by using 10% w/v FG/0.5% w/v TG. Hydrogel precursor solutions were mixed with fluorescent beads (shown in magenta) to visualize the gel volume. An automatic quality control analysis was performed to evaluate hydrogel morphology and check if the sample touched the well walls. 91% of the samples resulted in well-deposited planar hydrogels (green boxes), 6% of them formed a meniscus due to touching the walls (red boxes), while 3% of samples appeared with a concave shape (yellow boxes). "x" symbols on well shows wrong classification done by the automatic analysis. Well width: 3.7 mm. **(B)** 3D rendering of HaCaT cells (actin in gray) on the hydrogel surface (fluorescent beads in magenta). **(C)** 18-hour live fluorescence imaging experiment of HaCaT cells on hydrogels. HaCaT cells express fluorescent sensors for actin (in gray) and the cell cycle (cyan nuclei in G1 phase in cyan, nuclei in S/G2/M phase in magenta). Segmentation masks for selected cells and tracks backward in time are shown. Mask outlines were colored manually on TrackMate according to the cell cycle phase. A tracking diagram is shown where each spot represents a cell at a specific phase of the cell cycle at each time point. The dashed white box indicates the tracking lineage of the highlighted cells. **(D)** Max intensity projections of the XY, XZ, and YZ planes from a z-stack showing a cluster of cells on hydrogels (actin in gray, tubulin in green, nuclei in cyan and magenta). (**i**) Red squared box zooms in on three cells undergoing mitosis, evidenced by mitotic spindles in green. (**ii**) White dashed box shows the actin and tubulin structures of cells well spread on the hydrogel surface. Zooms were adjusted by applying a Sharpening filter in FIJI[46]. Scale bars: 25 µm.

3 Discussion

In this study, we asked, *"What would it look like if it were simple to have biomimetic elements in HTS?"* Our answer is HYDRA, a scalable and automated approach for fabricating thin hydrogel films at the bottom of commercial HTS plates (**Figure 1**). Throughout this paper, we sought materials composition and fabrication strategies that would be simple to implement in industry-level scenarios, not in a research lab.

We chose cold fish gelatin as the main ECM component (**Figures 2A, 2E-F**) instead of more commonly used mammalian gelatins. Mammalian gelatin is utilized in manual casting or 3D printing due to its viscous nature at RT, which can be further tuned with a temperature-controlled print-head[27]. While we could have adopted a similar strategy, we preferred standard liquid handling equipment and sought a gelatin composition that would remain liquid at RT. While fish and mammalian collagens have several differences in their tertiary and quaternary structures, their denatured products – gelatins – are much more similar.[27,28] Our rheological studies demonstrated that the viscosity of fish gelatin at RT can be effectively handled using air displacement pipettes, even at elevated protein concentrations (**Figure 2B**). Moreover, the dispensed layer can be effectively cross-linked by microbial TG in a physiological range of stiffness (**Figure 2E-F**). This suggests this strategy can be used as-is in applications with a desired cell-adhesive hydrogel. However, our method could be extended to other materials with liquid hydrogel precursors (also photo-cross-linkable) to adjust the hydrogel stiffness and cell-binding properties, like hyaluronic acid, alginate, or methacryloyl fish gelatin.[47–49]

We approached the fabrication process similarly: *"What could be the easiest way to cast hydrogels in HTS plates for the pharmaceutical industry?"* The HYDRA manufacturing process is simple and involves dispensing a small volume of the hydrogel precursor solution at the center of each well, followed by re-aspirating the same liquid volume (**Figures 1A and B**). After dispensing the liquid and wetting the well bottom, a small amount of the hydrogel precursor will remain adhered to the glass/plastic, ensuring a thin hydrogel layer can be crosslinked in place. Here, the HYDRA method was demonstrated considering wells of standard 96- (**Figure 3**) and 384-well plates (**Figure 6**) with minimal hydrogel modifications. 1536 well plates should also be possible with the appropriate liquid handling robots, as long as

liquid dispensing does not contact the walls of each well and a boundary gel layer can be left after re-aspiration.

Next, we sought to validate HYDRA in challenging applications from a microscopy standpoint: we reasoned that introducing a hydrogel layer could impact imaging performances and placed ourselves in the most pessimistic scenario by casting the gelatin hydrogel in a plastic 96-well plate. Even under these conditions, we demonstrated the suitability of HYDRA HTS plates in digital holography (**Figure 4**) and fluorescence microscopy (**Figure 5**) on human epithelial cells engineered with various fluorescent sensors and treated with two drugs. Finally, we used imaging-grade 384-well plates with a COC backing to perform advanced live-cell and high-resolution confocal imaging on cells cultured on HYDRA gels (**Figure 6C-D**). The extra layer at the bottom of the plate did not affect standard imaging instruments, and the data quality was sufficient to automate data analysis in ways similar to current state-of-the-art cell painting assays and image analysis pipelines.[16,17]

The main limitation we see for HYDRA is the residual presence of a glass/plastic rim at the edge of the gel. This strong edge effect can easily be dealt with in imaging experiments by acquiring data only from the gel area. However, having cells on the glass/plastic rim remains problematic when extracting DNA, RNA, or proteins from the well, as the cells outside the gel may have distinct properties from the ones on the gel. Compared to the layer-by-layer and photo-crosslinking approaches for obtaining hydrogels in HTS plates, we traded well coverage in favor of physiologically relevant thickness and high-res imaging compatibility.[20,21] Since the final plate remains optically and chemically addressable, combining these and other approaches to generate full-well, more complex microenvironments in future versions of HYDRA will be possible.[47–49]

4 Conclusion

We developed HYDRA, a fully automated protocol to fabricate thin and planar hydrogels in standard HTS well plates. We used microbial transglutaminase-crosslinked fish gelatin as a cost-effective solution to create tissue-mimicking environments with tunable gel properties and high compatibility with liquid handling automation. We achieved planar gel profiles by exploiting contact angle hysteresis during liquid re-aspiration and surface dewetting. We validated this approach using imaging technologies and bioimage analyses relevant to HTS. Our approach can be easily integrated into a standard pharmaceutical pipeline as it uses nothing but readily available instruments and reagents in their expected context of use. Therefore, HYDRA has the potential to significantly improve the predictivity of pre-clinical trials in drug R & D by providing better mimicking substrates with a cost-effective and HTS-ready solution.

5 Experimental Section

Preparation of transglutaminase-crosslinked fish gelatin hydrogels. To prepare FG stock solutions, FG (gelatin from cold water fish skin, G7041-500G, Merck) was dissolved into Dulbecco's phosphate buffered saline (PBS) without Ca^{2+} and Mg^{2+} (referred to as "PBS -/-," C-40232, PromoCell). The solution was heated to 50 °C and magnetically stirred (between 700 and 800 rpm) for at least 30 min using a hotplate stirrer until gelatin was fully dissolved. The gelatin solution is filtered through a 0.45 µm filter (product number 514-1265, VWR). To enzymatically crosslink gelatin, TG powder (Activa® TI Transglutaminase, 1002, Modernist Pantry) was dissolved in PBS -/-, vortexed (between 700 and 800 rpm) for at least 10 minutes until fully dissolved, and then filtered through a 0.45 µm filter. FG and TG solutions were readily used after filtering or stored at 4 °C and used within one week. To explore the thickness and flatness of robot-cast hydrogels, samples were prepared with a gelatin content of 0.2 g mL^{-1} (20% w/v), 0.1 g mL^{-1} (10% w/v), and 0.05 g mL^{-1} (5% w/v) while keeping a constant TG concentration of 0.02 g mL^{-1} (2% w/v). To obtain 5% and 10% w/v FG hydrogels, doubly concentrated stock solutions of FG (10% and 20% w/v, respectively) and 4% w/v TG solution were prepared and then mixed at a 1:1 ratio. Instead, 20% w/v FG hydrogels were prepared using a 25% w/v gelatin stock solution and a 10% w/v TG and mixed at a 4:1 ratio. After mixing, the resulting hydrogel precursor solution was placed in a cell incubator (37 °C, 100% humidity, 5% CO_2) for overnight crosslinking. During crosslinking in the incubator, a water reservoir was placed with the plate in a sealed box in the incubator to maintain humidity control. The hydrogels were cast according to the experiment requirements and sterilized for one hour using a cell culture hood's ultraviolet (UV) light when used for cell culture. Subsequently, the gels were immersed in PBS -/- and stored at room temperature until cell seeding. To cast hydrogels in 384- (product number 781866, GREINER) and 1536-well plates (product number 4561, Corning) a precursor solution containing 0.1 g mL^{-1} gelatin (10% w/v), and 0.005 g mL^{-1} TG (0.5% w/v) was prepared.

Rheological characterization of hydrogel viscosity and stiffness.

The tube inversion method was used to study the physical and chemical gelation of FG. Three FG concentrations (5% w/v, 10% w/v, and 20% w/v in PBS -/-) were pre-mixed with TG[28]. The mixture was manually dispensed into microcentrifuge tubes, which were then kept at room

temperature and 4 °C for 72 hours (n=3). Images were taken of the inverted tubes at 24, 48, and 72 hours to assess gelation (**Figure S1**).

The rheological measurements were performed using a Discovery HR-2 rheometer (TA Instruments) with plate-plate geometry and a Peltier solvent trap to prevent water evaporation. To verify the compatibility with automated pipetting, the viscosity of the hydrogel precursors was characterized by flow sweep measurement at room temperature for varying FG concentrations, from 5 to 20% w/v, by pipetting 150 uL of FG solution directly on the plate. For assessing the shear modulus (stiffness) of various formulations, samples were prepared one day before the measurements after overnight crosslinking at 37 °C. Hydrogels with varying FG concentrations were shaped into cylinders about 2 mm high and having diameters of 2 cm. The cylinders were prepared by casting the hydrogel precursor solution on a glass microscope slide and shaped into cylinders using glass coverslips as lateral spacers and a passivated coverslip on top. Time sweep measurements were carried out at constant strain (1%) and frequency (1 Hz), at 37 °C. Dynamic amplitude measurements were performed at a constant frequency (1 Hz), at increasing strain (0.1-1000%), at 37 °C. Gelation measurements were performed on hydrogel precursor formulations, by pipetting 150 uL of solution on the plate (strain 1%, frequency 1 Hz) (**Figure 2, S2, and S3**).

Computational Fluid Dynamics simulations. COMSOL Multiphysics (version 6.1, COMSOL) was used to explore the possibility of producing planar 2.5D hydrogels by simulating the process of dispensing and aspiration by a pipette tip in the center of a cylindrical well. Specifically, the "*Laminar Two-Phase Flow, Phase Field*" interface (including gravity contribution) was used to track the interface between the hydrogel precursor solution and air. Since the system under consideration (pipette at the center of a well) is symmetric, a 2D axisymmetric geometry was chosen to save computational power and time. In the 2D geometry, the well was modeled as a rectangle of dimensions R_w and H_w (**Figure S4 and Table S1**), with "*wetted wall boundary*" conditions imposed for the bottom and sidewall boundaries of the well and "*open boundary*" condition at the top of the well, since the upper part of the well is open. In the *"wetted wall"* condition, the contact angle hysteresis was modeled using advancing and receding angle values reported in the literature (**Table S1**).[50] Specifically, the angle at the wetted wall was set as "advancing" when the contact line velocity, the velocity at which the fluid moves at the bottom of the well, was positive and as "receding" when it was negative. The pipette was modeled as a rectangle of dimensions R_p and H_p (**Figure S4 and Table S1**),

with an "*interior wetted wall*" condition at the lateral wall of the pipette, inside the well domain. An *"inlet"* condition was applied at the upper edge of the pipette to simulate dispensing and aspiration by using positive and negative *"fully developed flow,"* respectively. The properties of "air" and "water" imported from the COMSOL material library were assigned to the well and pipette domains, respectively. To model the hydrogel precursor solution in the selected COMSOL interface, the viscosity for the liquid phase was set at the value for the 10% w/v hydrogel precursor solution found in this study. The density and surface tension were set respectively at the nominal value for water and the value found in the literature for FG.[51] The mesh was created using the "*physics-controlled*" option with an *"extra fine"* mesh size. Gel flatness at the end of the simulation was assessed by evaluating the angle at every profile point, which was directly calculated in COMSOL. The air-liquid interface was considered "planar" when the angle concerning the pipette axis was 90° ± 3°. Flatness was calculated as the percentage of the length of the "planar" air-liquid interface over the well radius. To assess the occurrence of wall wetting for the different dispensed volumes, a parametric sweep was performed using a variation of ± 20% on the dispensed volume and a variation of -100 µm (if we consider separately the contribution of plate tolerance dimension and robot calibration) and -200 µm (if we consider the sum of the two contributes) on the well radius.

Hydrogel fabrication using liquid handling robots. An open-source pipetting system (OT-2 robot, Opentrons) was used to explore the fabrication feasibility of micrometric-thick planar hydrogels. Specifically, a liquid handling robot pipeline was implemented using the Opentrons Protocol Designer (Version 7.0.0, Opentrons) to cast and re-aspirate the hydrogel precursor solutions, leaving planar cylindrically shaped hydrogels on the plastic substrates. In terms of hardware, the robot uses a removable P300 single-channel Gen2 pipette (in short "P300") mounted and a P20 single-channel Gen2 pipette (in short "P20"), an Eppendorf vial rack for the stock solutions (Opentrons), and 8-well plates (µ-Slide 8 Well High ibiTreat, 80806, Ibidi) as receiving plastic substrate. Before casting, the system was calibrated to account for the pipette lengths and the positions of the remaining hardware (vials and the receiving substrate). During casting, the hydrogel precursor solution was prepared by mixing the stock solutions (detail in the "Preparation of TG-crosslinked FG hydrogels" section) into a new Eppendorf vial using P300 and a different tip for each solution. Then, the hydrogel solution was cast into an 8-well plate using an individual P20 tip for each gel. Specifically, the pipette was programmed to dispense 12 µL of liquid at 500 µm from the well bottom with a flow rate of 0.5 µL s^{-1} and

aspirate the same volume at 100 µm from the well bottom with a flow rate of 0.1 µL s^{-1}. To test the HYDRA method in low throughput plates, a custom protocol in Python was developed using P300 and P20 pipettes, an Eppendorf tube rack for the stock solutions (Opentrons), and 12-well plates (11012, BIOFIL) as the plastic substrate. Initially, the precursor solutions were pre-mixed in a new tube rack using the P300 pipette. HYDRA-like hydrogels were cast in the first half of the 12-well plate using a volume of 200 µL each. After re-mixing the precursor solutions, a P20 pipette was used to cast multiple 20 µL gels in each well of the second half of the plate. To visualize the final gels, 18 µL were aspirated from each gel (**Figure S11C**).

Scalable hydrogel fabrication using a multichannel system. To prove hydrogel fabrication in a scalable fashion, FG hydrogels were fabricated in a 96-well plate to a robot compatible with cell culture hood operation and equipped with multichannel pipettes. Specifically, an Assist Plus robot (Integra Biosciences) with a 3-position deck (product number 4520, Integra Biosciences) and two 8-channel pipettes, namely a 300 µL and a 12.5 µL 8-channel VOYAGER pipettes (respectively, product numbers 4723 and 4721, Integra Biosciences), were used. In this case, two sequential protocols were developed using VIALAB software (Version 3.1.2.0, Integra Biosciences). In brief, the first protocol uses the 300 µL 8-channel pipette to mix FG and TG solutions and cast the hydrogel precursor solution in an 8-element row of Eppendorf vials. After manually replacing the 300 µL pipette with a 12.5 µL 8-channel pipette, the second protocol cast the previously mixed hydrogel solution into a 96-well plate (product number 83.3924, Sarstedt). The 8-channel pipette was programmed to dispense 12 µL of hydrogel solution and then aspirate the same amount of liquid one column at a time. Before dispensing, a step of pre-mixing was always performed (**Figure 3C and Video s3, s4**). Two additional 96-well plates (product number 89626, IBIDI) were prepared using the same settings to evaluate fish gelatin hydrogel degradation over time. After cross-linking, these plates were rehydrated in PBS, sealed with parafilm (product number PM-992, Bemis), and stored at 4°C for up to two months, respectively. At these specific times, engineered HaCaT cells expressing a fluorescent marker for actin were seeded on the gels to assess hydrogel degradation. Static widefield images were captured using a Crest V3 X-Light spinning disk confocal microscope (Nikon) equipped with a Celesta Light Engine source (TSX5030FV, Lumencore), a Photometrics Kinetix Scientific CMOS camera, and an air 10X objective (NA 0.30) (MRH00105, Nikon) (**Figure S11A**). Lumencore CELESTA Light Engine with 546 nm (laser

power 16 ± 2 mW, exposure 200 ms) was used. One field of view per well was acquired automatically using the JOBS module of the Nikon NIS-Elements package.[52]

For the 384-well (product numbers 781866, GREINER and 4681, Corning) and 1536-well plates (product number 4561, Corning), a 12.5 µL 16-channel VIAFLO pipette (product number 4641, Integra Biosciences) was used to cast the hydrogel solution. In brief, 10% w/v FG and 0.5% w/v TG solutions were pre-mixed and dispensed into a 25 mL reservoir before running the protocol (product number 4310, Integra Biosciences). The 16-channel pipette was programmed to dispense 1 µL in the 384-well plate and 0.5 µL in the 1536-well plate of hydrogel solution. The robot then aspirated 0.5 µL for both plates, one column at a time (**Figure 6A, S10i, and ii**). To enable hydrogels to adhere to the glass surface, a standard protocol for low-throughput glass coverslips[25] was adapted to 96-well plates with a glass bottom (product number 89627, IBIDI). The protocol was created using the OT-2 robot placed under a chemical hood and the Opentrons Protocol Designer (Version 7.0.0, Opentrons). Briefly, the plate was treated as follows: firstly, with 0.1 M NaOH for 5 minutes, then with 0.5% APTMS (product number 475149-5ML, Sigma) in 95% ethanol for 5 minutes, and finally with 0.5% v/v glutaraldehyde for 30 minutes. Static BF images (time exposure 5 ms) were captured using a Crest V3 X-Light spinning disk confocal microscope (Nikon) equipped with a Celesta Light Engine source (TSX5030FV, Lumencore), a Photometrics Kinetix Scientific CMOS camera, and an air 4X objective (NA 0.13) (MRH00045, Nikon) to image the entire gel (**Figure S11B**). One field of view per well was acquired automatically using the JOBS module of the Nikon NIS-Elements package.[52] Images were flat-field corrected using BioVoxxel 3D Box FIJI[46] plugin.

Cell culture. HaCaT cells were kindly provided by Professor Hugo de Jonge (Department of Molecular Medicine, University of Pavia) and engineered to express multiple fluorescent proteins following a previously developed protocol.[24] Briefly, the cell cycle can be tracked through a genetic modification to express a variant of the FUCCI[53] sensor, called FUCCIplex that uses cyan (mTurquoise2) and far-red (miRFP670).[24] Actin and tubulin can be visualized through the expression of genetically encoded RFP-Life Act™ and genome-edited EGFP-tubulin, respectively. The engineered HaCaT cells were cultured in a conventional incubator (37 °C, 90% Humidity, 5% CO_2) using Dulbecco's modified Eagle's medium F-12 Nutrient Mixture (11320-074, Gibco), supplemented with 10% heat-inactivated fetal bovine serum (10270-106, Gibco), and 1% penicillin and streptomycin antibiotic solution (A001-100ML,

Himedia). Cells were consistently kept below confluency, and the splitting procedure was carried out when they reached 70% confluence.

Morphological characterization of robot-cast gels in hydrated states. To first evaluate the geometry of the hydrogels in the hydrated state, fluorescent beads were included in the hydrogel, and immortalized nontumorigenic human epidermal (HaCaT) cells expressing fluorescent proteins were seeded on top of the gels and the surrounding plastic substrate. To visualize the gel using fluorescence microscopy, the hydrogel precursors solution was supplemented with a fluorescent bead solution (Excitation 660 nm / Emission 680 nm, product number F8807, Thermo Fisher) with a 50:1 volume ratio. Hydrogels with 5%, 10%, and 20% w/v of gelatin were cast into the 8-well plate (µ-Slide 8 Well High ibiTreat, 80806, Ibidi) and left crosslinking overnight, as previously explained. The samples were then rehydrated in PBS -/- before cell seeding. To verify biocompatibility and allow morphological characterization of the hydrogels by fluorescence confocal microscopy, $5x10^5$ cells mL^{-1} genome-edited HaCaT cells were seeded. The RFP-Life Act™ construct (excited with 546 nm) was used for this experiment to visualize actin and obtain fiduciary points for assessing the gel profile and the plastic substrate. Static confocal images were captured on both the upper and lower surfaces of the gels using a Crest V3 X-Light spinning disk confocal microscope (Nikon) equipped with a Celesta Light Engine source (TSX5030FV, Lumencore), a Photometrics Kinetix Scientific CMOS camera, and an air 20X objective (NA 0.75) (MRD00205, Nikon). The z-level of the cells adhering on top of the gel and of the plastic substrate were recorded to evaluate the gel thickness and flatness (**Figure 3D, E, and S5**).

Automated quality control of HYDRA-like hydrogels in HTS plates. To evaluate hydrogel fabrication in 384-well (product number 781866, GREINER) and 1536-well plates (product number 4561, Corning), automated acquisition, and quality control analysis were implemented. The JOBS module of the Nikon NIS-Elements package (Nikon) was used to automate plate acquisition. Briefly, the microscope was programmed to acquire static z-stacks in widefield mode (z-step size of 30 µm) for each well of the plates at the center position. A Crest V3 X-Light spinning disk confocal microscope (Nikon) equipped with a Celesta Light Engine source (TSX5030FV, Lumencore), a Photometrics Kinetix Scientific CMOS camera, and an air 4X (NA 0.13) (MRH00045, Nikon) was used. Lumencore CELESTA Light Engine with 546 nm

(laser power 16 ± 2 mW, exposure 300 ms), and 638 nm (laser power 37 ± 4 mW, exposure 30 ms) wavelengths were used to image well walls and hydrogels embedding fluorescent beads, respectively (**Video s7**). A FIJI macro script was developed for quality control analysis of HYDRA-like gels in HTS plates. Initially, each image was cropped and rotated to center the well within the field of view. A maximum intensity projection was then obtained from the 2-channel stack input. The channels were processed separately as follows: for the well walls channel, a Gamma Correction (value=0.5) was applied, followed by an Auto-threshold ("Triangle" method with ImageJ's default settings). The same morphological operations (Opening, Closing, and Filling holes) and outlier removal (radius of 10 pixels) were performed, followed by edge detection using the "Find Edges" plugin. For the hydrogel channel, Auto-threshold ("Default" method with ImageJ's default settings), followed by morphological operations including "Opening," "Closing," and "Filling holes" were applied. Outliers were removed with a radius of 10 pixels using "Remove Outliers", and mask edges were detected using the "Find Edges" plugins in ImageJ. A logical "AND" operation was performed between the well wall mask and the first hydrogel mask to distinguish between gels that touched the walls forming a meniscus (in the script called "bad") or not. A second deeper analysis was done by processing the hydrogel max intensity projection image with a Gamma Correction (value=2) and auto-thresholding ("Default" method with ImageJ's default settings). A "Closing" morphological operation was applied, and the mask was analyzed using the ImageJ plugin "Analyze Particles". If the mean measured gray value of the thresholded mask was equal to or greater than 250, the hydrogel was classified as "planar"; otherwise, it was considered to have a "concave" shape. The image filename and the well classification ("bad"," planar", "concave") were saved in an Excel file. A Python script was used to generate the tiling of the wells. Using the filenames of the images and an Excel file containing the classification information, the well images were aligned and tiled. Each well image was overlaid with a colored frame based on the hydrogel classification: green for "planar," red for those that touched the walls, and yellow for "concave" (**Figure 6A, Figure S10i, ii, and Video s8**).

Profile extraction of fish gelatin hydrogels in a 384-well plate. Fluorescent beads were embedded in the hydrogels as previously described to evaluate the profiles of the hydrogels formed in the 384-well plate (product number 781866, GREINER). Following overnight crosslinking and PBS -/- rehydration, large field-of-view z-stacks were acquired using a Crest V3 X-Light spinning disk confocal microscope (Nikon). This setup included a Celesta Light

Engine source (TSX5030FV, Lumencore), a Photometrics Kinetix Scientific CMOS camera, and an air 20X objective (NA 0.75) (MRD00205, Nikon). A custom Python script was developed to extract planar and concave hydrogel profiles (n=3 for concave and n=5 for planar gels). Briefly, the z-stack images were processed by applying Otsu thresholding and morphological closing to each image stack to differentiate the gel from the background. The height of the gel was determined by the distance between the first and last detected signals in each plane, multiplied by the z-step size of 2 µm. A moving average filter of 15 pixels (approximately 10 µm, pixel-to-micrometer ratio = 0.67) was applied to smooth the profiles (**Figure S10A, B**).

Drug screening using digital holographic long-term imaging. Nocodazole (M1404-50MG, Merck) and paclitaxel (10461, Cayman Chemical) were chosen as test compounds. The drugs were dissolved in dimethylsulphoxide (D2650-100ML, Merck), aliquoted in 1 mL Eppendorf vial, and kept at -20 °C. 10% w/v FG-based culture platform was fabricated as described previously (see "Preparation of transglutaminase-crosslinked fish gelatin hydrogels" and "Automated hydrogel fabrication using liquid handling robots"). HaCaT cells (P50-P70, 50.000 cells/mL) were seeded on 10% w/v FG hydrogels 24 h before treatment by casting 100 µL per well of the 96-well plate. In the drug screening, cells were treated with three different concentrations per drug, and positive and negative controls (resulting in 12 replicates per group) were included. Specifically, nocodazole and paclitaxel (5 mg/mL) were diluted to 5 µg mL^{-1} solutions in a DMEM culture medium. Cells were treated with nocodazole concentrations of 12.5, 25, and 50 ng mL^{-1} and paclitaxel concentrations of 0.5, 2.5, and 12.5 ng mL^{-1}. Wells with 0.1% DMSO and 1500 µg mL^{-1} Geneticin (10131-027, Gibco) were used as a negative and positive control, respectively. After adding drugs, the 96-well plate was immediately placed on the motorized stage of a HoloMonitor M4 (Phase Holographic Imaging AB) inside a cell incubator (37 °C, 100% humidity, 5% CO_2). Using HoloMonitor Appsuite software (Version 4.0.1, Phase Holographic Imaging PHI AB), one field of view per well was selected and imaged every hour for 48 hours using an Olympus PLN 20X objective (NA 0.4) (N1215900, Evident) and a low-power laser unit (635 nm, 0.2 mW cm^{-2}). Time-lapse images were exported and processed on ImageJ FIJI software to extract the cell % confluency. In detail, the cell confluency was defined as the *sum of areas occupied by cells* / the *total size of the field of view*) (**Figure 4, S6, S7, S8, and Videos s5, s6**).

Drug screening using static widefield fluorescence imaging. As reported in the "Drug screening using digital holographic long-term imaging" section, an equivalent platform was used to capture static widefield images of cells on the gels at two time points: 24 and 48 hours after drug treatments. One image of each well was taken using the Ti2 inverted microscope (Nikon) equipped with an air 20X objective (NA 0.75) (MRD00205, Nikon). Lumencore CELESTA Light Engine with 546 nm (laser power 16 ± 2 mW, exposure 50 ms), 477 nm (laser power 28 ± 3 mW, exposure 50 ms), 446 nm (laser power 20 ± 2 mW, exposure 10 ms), and 638 nm (laser power 37 ± 4 mW, exposure 200 ms) wavelengths were used to image cell actin, tubulin, and nuclei in G1 or S/G2/M, respectively. The JOBS module of the Nikon NIS-Elements package (Nikon) was used to implement a semi-automatic acquisition protocol. Briefly, the JOB starts by placing the objective automatically at the well center at the left edge of the 96-well plate. Then, the focus is set manually using the 477 wavelength and recorded to acquire a 4-channel image. The step is repeated on each well of the 96-well plate. The entire protocol is executed twice, first to capture cells on hydrogel substrates and second to capture cells positioned on the plastic rim surrounding the gel (**Figure 5 and S9**).

Cell confluency analysis using digital holographic long-term imaging. To extract the cell confluency value (defined as the percentage of the field of view featuring cells), time-lapse datasets from the HoloMonitor microscope were exported from HoloMonitor Appsuite software (Version 4.0.1, Phase Holographic Imaging PHI AB) and processed using the open-source ImageJ FIJI software.[46] The images were processed as follows: "Non-local means (NML) denoising" ImageJ plugin (auto-estimated sigma, smoothing factor "1"),[54,55] Auto-threshold ("Triangle" method, default settings provided by ImageJ), morphological operators including "Opening," "Closing" and "Filling holes" operators (ImageJ) and Particle analysis ("Analyze Particles" ImageJ plugin) to extract "%Area" values, i.e., cell confluency values. Quantitative imaging in the phase domain is susceptible to artifacts that may affect cell confluency data. To address this issue, a moving average (window size 4) was applied to the time-series data analyzed automatically. Moreover, images were manually examined when the confluency was greater than 30%, a threshold at which automatic segmentation became much less accurate than manual segmentation (**Figure 4D, E, F, Figure S6, and S8**).

High-resolution live fluorescence imaging. Cells on gels cast in 384-well plates (product number 4681, Corning) were analyzed by long-term widefield acquisition and static confocal fluorescence imaging. For long-term widefield, one image was taken per well every 15 minutes for 18 hours (**Figure 6C and Video s9**). Three wells of the plate were considered. A Ti2 inverted microscope (Nikon) equipped with a 40X silicon oil objective (NA 1.25) (MRD73400, Nikon). Lumencore CELESTA Light Engine with 546 nm (laser power 16 ± 2 mW, exposure 200 ms), 477 nm (laser power 28 ± 3 mW, exposure 30 ms), 446 nm (laser power 20 ± 2 mW, exposure 10 ms), and 638 nm (laser power 37 ± 4 mW, exposure 60 ms) wavelengths were used to image cell actin, tubulin, and nuclei in G1 or S/G2/M, respectively. For high-resolution static imaging of cell clusters, confocal z-stacks (z-step size of 0.3 μm) was captured using a Crest V3 X-Light spinning disk confocal microscope (Nikon) equipped with a Celesta Light Engine source (TSX5030FV, Lumencore), a Photometrics Kinetix Scientific CMOS camera, and a 40X (NA 1.25) (MRD73400, Nikon) or 100X silicon oil objective (NA 1.35) (MRD73950, Nikon). AI Denoising and Richardson-Lucy deconvolution (50 iterations) processing were used in NIS-Elements software.[52] Z-stacks volumes were visualized as max intensity projections of the XY planes and orthogonal views (XZ, YZ) or as 3D rendering in NIS-Elements software (**Figure 6D**).[52]

Cell cycle analysis using fluorescence widefield imaging. Static widefield fluorescence images were analyzed to quantify the cell count in M phases. The tubulin (green) and nuclear (cyan and magenta) channels underwent individual preprocessing steps, including planar-field correction and denoising (median filtering). Magenta and cyan channels were summed to obtain a unified nuclear channel. This channel was used to segment cells using Stardist pre-trained (Versatile fluorescent nuclei) model.[45] The resulting regions of interest (ROIs) were used to measure the intensity values in the nuclei channels (**Figure 5 and S9**). Long-term widefield fluorescence videos were analyzed to quantify the cell cycle and to track cells over time. The actin (gray) and nuclear (cyan and magenta) channels were processed separately using non-local means denoising.[56] Nuclei segmentation by a pre-trained Stardist[45] neural network was manually curated: roughly 10% of the mask frames were corrected (**Figure 6C, D, and Video s9**).

A cell cycle phase classification method was applied as previously reported.[24] Briefly, the mean intensity values of the cyan and magenta channels were utilized to assign the cell phase to the detected nuclei. Background subtraction was performed for each channel, and a threshold

was set based on the maximum intensity value. Cells were classified as follows: if neither of the intensities exceeded the threshold, they were classified as being in the early G1 (EG1) phase; if either intensity surpassed the threshold, they were categorized as being in G1 (if the cyan channel exceeded the threshold) or S/G2/M phase (if the magenta channel exceeded the threshold). When both signals were above the threshold, cells were designated as being in the transition phase (T). Since mitotic cells could not be detected by the initially described algorithm[24], all cells were reassessed by evaluating tubulin intensity. Before this, the cyan channel was subtracted from the tubulin channel to eliminate bleed-through artifacts. The tubulin intensity outside the nuclei masks obtained from Stardist was utilized as an estimate of background intensity.[45] Cells were reclassified as being in the M phase if the tubulin intensity of a nucleus exceeded the background intensity by a factor of 0.2 (for plastic data) or 0.4 (for hydrogel data). These predetermined values were established to automate the classification analysis akin to expert manual evaluation. Notably, the tubulin threshold for hydrogel data was doubled compared to that for plastic to account for the autofluorescence background from the gel.

TrackMate was employed to track cells over time in long-term experiments. A TIFF file containing the label stack image, previously segmented using Stardist, was imported into TrackMate.[57] The label image detector was selected as the nuclei detector. LAP Tracker was configured with the following settings: a maximum distance of 50 µm for "frame-to-frame linking," "gap-closing" enabled with a maximum distance of 50 µm, and a “maximum frame gap” of 3 frames. "Future penalties" related to the mean intensity of nuclei channels set to 1. After tracking, lineage trees of the cells in the long-term videos were created with color-coded spots based on the position in the cell cycle (**Figure 6C**).[58] The linking of daughter cells was done manually. Around 5% of the spots were manually added after cell division, as the nuclear sensor is inactive in the early stages of the G1 phase.

Statistical analysis. Statistical analysis was carried out in GraphPad Prism 10 (GraphPad Software, USA). Mann Whitney multiple tests were performed to compare the confluency in long-term time series and static images. All the results are presented as mean ± standard error of the mean (s.e.m.).

Supporting Information

Supporting Information is available from the Wiley Online Library or the author.

Acknowledgments

This work was supported by the European Research Council (ERC) Starting Grant No. 852560 to F.S.P. and by the Italian Ministry of Education, University, and Research (MIUR) (FARE2020, Grant No. R20ZE54CTK) to F.S.P.

REFERENCES

[1] S. Harrer, P. Shah, B. Antony, J. Hu, *Trends in Pharmacological Sciences* **2019**, *40*, 577.
[2] M. Moor, O. Banerjee, Z. S. H. Abad, H. M. Krumholz, J. Leskovec, E. J. Topol, P. Rajpurkar, *Nature* **2023**, *616*, 259.
[3] C. Caudai, A. Galizia, F. Geraci, L. Le Pera, V. Morea, E. Salerno, A. Via, T. Colombo, *Comput Struct Biotechnol J* **2021**, *19*, 5762.
[4] M. S. Ringel, J. W. Scannell, M. Baedeker, U. Schulze, *Nat Rev Drug Discov* **2020**, *19*, 833.
[5] J. W. Scannell, A. Blanckley, H. Boldon, B. Warrington, *Nature Reviews Drug Discovery* **2012**, *11*, 191.
[6] E. W. Esch, A. Bahinski, D. Huh, *Nature Reviews Drug Discovery* **2015**, *14*, 248.
[7] M. Kapałczyńska, T. Kolenda, W. Przybyła, M. Zajączkowska, A. Teresiak, V. Filas, M. Ibbs, R. Bliźniak, Ł. Łuczewski, K. Lamperska, *Arch Med Sci* **2018**, *14*, 910.
[8] Y. Fang, R. M. Eglen, *SLAS Discovery* **2017**, *22*, 456.
[9] I. Decoene, G. Nasello, R. F. Madeiro de Costa, G. Nilsson Hall, A. Pastore, I. Van Hoven, S. Ribeiro Viseu, C. Verfaillie, L. Geris, F. P. Luyten, I. Papantoniou, *Stem Cells Translational Medicine* **2024**, szad091.
[10] S.-Y. Lee, H. J. Hwang, D. W. Lee, *Sci Rep* **2022**, *12*, 18937.
[11] Sonia Youhanna, Aurino M. Kemas, Lena Preiss, Yitian Zhou, Joanne X. Shen, Selgin D. Cakal, Francesco S. Paqualini, Sravan K. Goparaju, Reza Zandi Shafagh, Johan Ulrik Lind, Carl M. Sellgren, Volker M. Lauschke, *Pharmacol Rev* **2022**, *74*, 141.
[12] M. Nikolaev, O. Mitrofanova, N. Broguiere, S. Geraldo, D. Dutta, Y. Tabata, B. Elci, N. Brandenberg, I. Kolotuev, N. Gjorevski, H. Clevers, M. P. Lutolf, *Nature* **2020**, *585*, 574.
[13] C. Quintard, E. Tubbs, G. Jonsson, J. Jiao, J. Wang, N. Werschler, C. Laporte, A. Pitaval, T.-S. Bah, G. Pomeranz, C. Bissardon, J. Kaal, A. Leopoldi, D. A. Long, P. Blandin, J.-L. Achard, C. Battail, A. Hagelkruys, F. Navarro, Y. Fouillet, J. M. Penninger, X. Gidrol, *Nature Communications* **2024**, *15*, 1452.
[14] D. Rodoplu, J. S. Matahum, C.-H. Hsu, *Lab Chip* **2022**, *22*, 1275.
[15] A. Skardal, S. V. Murphy, M. Devarasetty, I. Mead, H.-W. Kang, Y.-J. Seol, Y. Shrike Zhang, S.-R. Shin, L. Zhao, J. Aleman, A. R. Hall, T. D. Shupe, A. Kleensang, M. R. Dokmeci, S. Jin Lee, J. D. Jackson, J. J. Yoo, T. Hartung, A. Khademhosseini, S. Soker, C. E. Bishop, A. Atala, *Sci Rep* **2017**, *7*, 8837.
[16] S. Lin, K. Schorpp, I. Rothenaigner, K. Hadian, *Drug Discovery Today* **2020**, *25*, 1348.
[17] S. Kamiloglu, G. Sari, T. Ozdal, E. Capanoglu, *Food Frontiers* **2020**, *1*, 332.
[18] S. R. Caliari, J. A. Burdick, *Nature Methods* **2016**, *13*, 405.
[19] O. J. Trask, *Methods Mol Biol* **2018**, *1683*, 75.
[20] E. A. Brooks, L. E. Jansen, M. F. Gencoglu, A. M. Yurkevicz, S. R. Peyton, *ACS Biomater. Sci. Eng.* **2018**, *4*, 707.
[21] P. Machillot, C. Quintal, F. Dalonneau, L. Hermant, P. Monnot, K. Matthews, V. Fitzpatrick, J. Liu, I. Pignot-Paintrand, C. Picart, *Advanced Materials* **2018**, *30*, 1801097.
[22] A. Buxboim, K. Rajagopal, A. E. X. Brown, D. E. Discher, *Journal of Physics: Condensed Matter* **2010**, *22*, 194116.
[23] Y. Atma, *BIOINTERFACE RESEARCH IN APPLIED CHEMISTRY* **2022**, *12*, 3966.
[24] M. Di Sante, M. Pezzotti, J. Zimmermann, A. Enrico, J. Deschamps, E. Balmas, S. Becca, A. Reali, A. Bertero, F. Jug, F. S. Pasqualini, *bioRxiv* **2024**, 2024.12.19.629259.
[25] M. L. McCain, A. Agarwal, H. W. Nesmith, A. P. Nesmith, K. K. Parker, *Biomaterials* **2014**, *35*, 5462.
[26] J. H. Jensen, S. D. Cakal, J. Li, C. J. Pless, C. Radeke, M. L. Jepsen, T. E. Jensen, M. Dufva, J. U. Lind, *Scientific Reports* **2020**, *10*, 13305.
[27] I. J. Haug, K. I. Draget, O. Smidsrød, *Food Hydrocolloids* **2004**, *18*, 203.
[28] Y.-J. Kim, H. Uyama, *Polymer Journal* **2007**, *39*, 1040.

[29]"Viscous Liquids Need Special Pipetting Techniques - Eppendorf Handling Solutions," can be found under https://handling-solutions.eppendorf.com/liquid-handling/pipetting-facts/pipetting-of-challenging-liquids/detailview/news/viscous-liquids-need-special-pipetting-techniques/?utm_source=twitter&utm_medium=link&utm_campaign=hq%3Bbasicnoise%3Btraffic&utm_term=custom%3Bsingle_image%3Bunspecified&utm_content=glo%3Ben%3Bunspecified%3Bunspecified%3Bunspecified, **2018**.
[30]A. Lu, J. Zhu, G. Zhang, G. Sun, *J. Mater. Chem.* **2011**, *21*, 18674.
[31]A. Sancakli, B. Basaran, F. Arican, O. Polat, *SN Applied Sciences* **2021**, *3*, 8.
[32]K. Song, B. Ren, Y. Zhai, W. Chai, Y. Huang, *Biofabrication* **2021**, *14*, DOI 10.1088/1758-5090/ac3d75.
[33]F. Bode, M. A. da Silva, A. F. Drake, S. B. Ross-Murphy, C. A. Dreiss, *Biomacromolecules* **2011**, *12*, 3741.
[34]Y. Sui, H. Ding, P. D. M. Spelt, *Annual Review of Fluid Mechanics* **2014**, *46*, 97.
[35]K. Hokeness, L. H. Qiu, M. Vezeridis, B. F. Yan, S. Mehta, Y. S. Wan, *Oncol Rep* **2005**, *13*, 965.
[36]H.-E. Kim, H. Cho, A. Ishihara, B. Kim, O. Kim, *BMB Rep* **2018**, *51*, 188.
[37]M. Gustafsson, M. Sebesta, *Appl. Opt.* **2004**, *43*, 4796.
[38]M. Hellesvik, H. Øye, H. Aksnes, *Scientific Reports* **2020**, *10*, 14680.
[39]S. R. Caliari, J. A. Burdick, *Nature Methods* **2016**, *13*, 405.
[40]Cooper GM., in *The Cell: A Molecular Approach*, Sunderland (MA): Sinauer Associates, **2000**.
[41]N. Sharma, Z. Kosan, J. Stallworth, N. Berbari, B. Yoder, *Molecular biology of the cell* **2011**, *22*, 806.
[42]V. Goler-Baron, Y. G. Assaraf, *PLOS ONE* **2011**, *6*, e16007.
[43]A. Elfarnawany, F. Dehghani, *Toxics* **2023**, *11*, DOI 10.3390/toxics11070581.
[44]S. Seal, M.-A. Trapotsi, O. Spjuth, S. Singh, J. Carreras-Puigvert, N. Greene, A. Bender, A. E. Carpenter, **2024**.
[45]U. Schmidt, M. Weigert, C. Broaddus, G. Myers, in *Medical Image Computing and Computer Assisted Intervention – MICCAI 2018* (Eds.: A. F. Frangi, J. A. Schnabel, C. Davatzikos, C. Alberola-López, G. Fichtinger), Springer International Publishing, Cham, **2018**, pp. 265–273.
[46]J. Schindelin, I. Arganda-Carreras, E. Frise, V. Kaynig, M. Longair, T. Pietzsch, S. Preibisch, C. Rueden, S. Saalfeld, B. Schmid, J.-Y. Tinevez, D. J. White, V. Hartenstein, K. Eliceiri, P. Tomancak, A. Cardona, *Nature Methods* **2012**, *9*, 676.
[47]L. Gao, R. Beninatto, T. Oláh, L. Goebel, K. Tao, R. Roels, S. Schrenker, J. Glomm, J. K. Venkatesan, G. Schmitt, E. Sahin, O. Dahhan, M. Pavan, C. Barbera, A. D. Lucia, M. D. Menger, M. W. Laschke, M. Cucchiarini, D. Galesso, H. Madry, *Advanced Healthcare Materials* **2023**, *12*, 2300931.
[48]A. Agarwal, Y. Farouz, A. P. Nesmith, L. F. Deravi, M. L. McCain, K. K. Parker, *Advanced Functional Materials* **2013**, *23*, 3738.
[49]H. Yoon, S. Shin, J. Cha, S.-H. Lee, J.-H. Kim, J. T. Do, H. Song, H. Bae, *PLOS ONE* **2016**, *11*, e0163902.
[50]I. Beaulieu, M. Geissler, J. Mauzeroll, *Langmuir* **2009**, *25*, 7169.
[51]N. Phawaphuthanon, D. Yu, P. Ngamnikom, I.-S. Shin, D. Chung, *Food Hydrocolloids* **2019**, *88*, 119.
[52]"NIS-Element," can be found under https://www.nikoninstruments.com/Products/Software, **n.d.**
[53]A. Sakaue-Sawano, H. Kurokawa, T. Morimura, A. Hanyu, H. Hama, H. Osawa, S. Kashiwagi, K. Fukami, T. Miyata, H. Miyoshi, T. Imamura, M. Ogawa, H. Masai, A. Miyawaki, *Cell* **2008**, *132*, 487.
[54]B. Coll, J.-M. Morel, *Image Processing On Line* **2011**, *1*, DOI 10.5201/ipol.2011.bcm_nlm.
[55]J. Darbon, A. Cunha, T. F. Chan, S. Osher, G. J. Jensen, in *2008 5th IEEE International Symposium on Biomedical Imaging: From Nano to Macro*, **2008**, pp. 1331–1334.
[56]M. Weigert, "gputools: OpenCL accelerated volume processing," can be found under https://github.com/maweigert/gputools, **n.d.**
[57]J.-Y. Tinevez, N. Perry, J. Schindelin, G. M. Hoopes, G. D. Reynolds, E. Laplantine, S. Y. Bednarek, S. L. Shorte, K. W. Eliceiri, *Methods* **2017**, *115*, 80.
[58]Leo Guignard, "LineageTree," can be found under https://github.com/GuignardLab/LineageTree, **n.d.**